Corrosion Science 219 (2023) 111203

Contents lists available at ScienceDirect

Corrosion Science

journal homepage: www.elsevier.com/locate/corsci

Microstructures and high temperature oxidation behaviors of $AlMo_{0.5}NbTa_{0.5}TiZr$ high entropy alloys coated by silicon pack cementation

C. Hwang, K.P. Shinde *, J. Oh, S. Lee, C.H. Chung, J.S. Park *

Department of Materials Science and Engineering, Hanbat National University, Daejeon 34158, the Republic of Korea

ARTICLE INFO

Keywords:
High entropy alloy
Oxidation
Microstructure
Coatings
Pack cementation

ABSTRACT

In this study, we fabricated silicon coatings on $AlMo_{0.5}NbTa_{0.5}TiZr$ refractory high entropy alloy using pack cementation for the first time. The growth kinetics of the coating layer were analyzed by considering coating temperature, time, amount of Si, and NaF. The growth coefficient constant and activation energy were determined to be 96,823 μm/$h^{1/2}$ and 117 kJ/mol, respectively. Microstructural analysis revealed the formation of a protective layer of SiO_2 on the specimen surface, which increased its oxidation resistance at 1300 °C. Comparing the uncoated and coated specimens provided insight into the potential use of $AlMo_{0.5}NbTa_{0.5}TiZr$ for high-temperature applications.

1. Introduction

The excellent mechanical properties of high-entropy alloys (HEAs) have attracted extensive interest within the scientific community in materials science. However, understanding their oxidation resistance at high temperatures is also an important issue. For high-temperature applications, HEAs consist of five or more principle equi-atomic elements [1–5] and are classified into two groups: 3-d transition metals (*Ni, Mn, Ti, Co, Cr, Cu*)-based and refractory elements (*W, Ta, Re, Mo, Nb, Hf*)-based, commonly known as refractory high-entropy alloys (RHEAs) [6]. Due to their high melting point, solid solution strengthening, and lightweight, refractory HEAs exhibit superior mechanical properties over conventional Ni-based superalloys at high temperatures, which makes them highly desirable for aerospace and marine industry applications [7–10]. The various combinations of elements, including MoNbHfZrTi [11], HfNbTaTiZr [12], TiNbTaZr [13], MoNbTaVW [14], AlNbTiZr [15], NbTaTiV [16], and NbMoTaW [17], have been recently reported for their mechanical and oxidation properties.

The AlMoNbTaTiZr-based system has recently gained significant attention in the development of refractory high entropy alloys, owing to its potential for use in high-temperature applications [18,19]. However, its poor oxidation resistance at higher temperatures restricts its application, leading researchers to explore anti-oxidation coatings. Cheng et al. [20] reported the fabrication of ceramic coatings on $AlTiNbMo_{0.5}Ta_{0.5}Zr$ by micro arc oxidation. The coating was composed of SiO_2 and Ta_2O_5, and it was found that the oxidation resistance of the alloy remarkably improved after the oxidation test at 1200 °C. Lu et al. [21] reported on the effect of adding Yttrium (*Y*) on the oxidation resistance of $AlMo_{0.5}NbTa_{0.5}TiZr$ refractory high entropy alloys. The addition of Yttrium resulted in the formation of $AlNbO_4$ based complex oxide, which led to a power law dependence of weight gain in oxidation tests. The addition of 0.6 at% Y exhibited better oxidation resistance at 800–1000 °C, but adding 1 at% *Y* had an adverse effect on oxidation tests due to the formation of local stress and cracks. Moreover, the systematic effect of *Al* element on the oxidation behavior of the refractory high entropy alloy $AlMo_{0.5}NbTa_{0.5}TiZr$ at 1000 °C was studied. The higher content of *Al* resulted in the formation of $AlNbO_4$ and $AlTaO_4$ instead of Nb_2O_5 and Ta_2O_5, improving the oxidation resistance of the alloys [22,23]. In the literature, the different coatings approaches were used such as formation of protective oxide layer, chemical vapor deposition [24], laser cladding [25,26], pack cementation [27–29], and slurry coatings [30] on refractory high entropy alloys but each techniques have drawbacks such as slurry technique negative effect of reducing alloy strength and ductility. Among the different coating techniques, silicide coatings perform exceptionally well in terms of oxidation performance at high temperatures above the 1200 °C. Recently, fabrication and oxidation behavior RHEAs $(NbMoTaW)Si_2$ coatings was reported by Kuang et al. [31]. The Si pack cementation technique was used for coating and excellent oxidation resistance was found for coated specimen compared with NbMoTaW alloy specimen at 1300 °C in air. Similarly, Yi et al. [17] also fabricated and studied oxidation resistance of $(NbMoTaWV)Si_2$ and substrate and analyzed

* Corresponding authors.
E-mail addresses: yourkirans@gmail.com (K.P. Shinde), jsphb@hanbat.ac.kr (J.S. Park).

https://doi.org/10.1016/j.corsci.2023.111203
Received 28 November 2022; Received in revised form 17 April 2023; Accepted 19 April 2023
Available online 25 April 2023

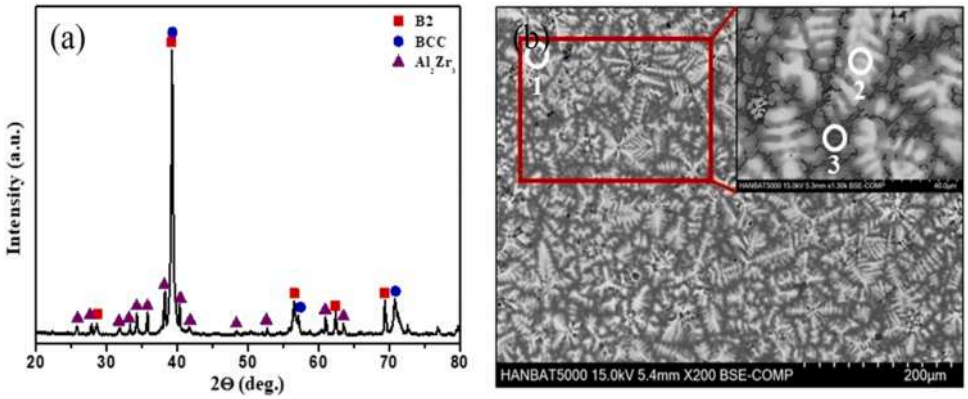

Fig. 1. (a) XRD pattern (b) BSE image of as casted $AlMo_{0.5}NbTa_{0.5}TiZr$ alloy.

Table 1
EDS analysis data of $AlMo_{0.5}NbTa_{0.5}TiZr$ alloy.

at%	*Al*	*Mo*	*Nb*	*Ta*	*Ti*	*Zr*
1	18.5	9.0	22.3	8.1	21.6	20.2
2	8.8	16.7	29.9	21.4	14.9	8.0
3	27.8	4.7	11.5	2.1	16.3	37.3

microstructure systematically. The high oxidation resistance in case of coated specimen was attributed to formation of dense SiO_2 layer at the interface.

The literature contains several coating models that predict the thickness of the coating layer. Majumdar et al. analyzed the coating kinetics of a *Mo*-based alloy using *Si* as a coating source and NH_4F as an activator at 800–1200 °C for up to 25 h [32]. Xiang et al. studied the *Fe*-based alloy P92 (12Cr-1Mo) coated with *Al* at 500–700 °C for up to 16 h using *Al* as the coating source and $AlCl_3$ as an activator. They proposed a coating model to predict the thickness of the coating layer and understand coating dynamics [33]. Choi et al. coated *Mo-3Si-B* alloy at 900–1100 °C for up to 48 h and presented a coating model using Si and NaF as the coating source and activator inside the pack [29]. All these models were based on the Levin and Caves model [34]. The growth of the coating layer was predicted through actual experimentation and theoretical calculations based on changes in the content of the coating source and activator (Si and NaF) inside the pack.

In this study, we report the fabrication of Si coatings on $AlMo_{0.5}NbTa_{0.5}TiZr$ refractory high-entropy alloy for the first time using the pack cementation method. The alloy was prepared by arc melting, and the pack cementation method was chosen due to its advantages, such as easy application on complex surfaces and excellent adhesion to the base material. Silicon powder was used as the coating source, and a coating layer was formed on the alloy surface through pack cementation coating. The growth kinetics of the coating layer, in terms of the content of *Si* used as the coating source and NaF used as an activator, were studied experimentally and theoretically. The post-coating structure and microstructure analyses were performed before and after oxidation tests at 1300 °C for up to 100 h. We discussed the comparison of uncoated and coated specimens through mass increase analysis due to the oxide layer formation after oxidation tests and microstructure studies.

2. Experimental

The refractory high entropy alloys (HEAs) containing $AlMo_{0.5}NbTa_{0.5}TiZr$ were synthesized by arc melting high purity *Al, Mo, Nb, Ta, Ti*, and *Zr* elements (> 99.9 %) in an Ar atmosphere inside a water-cooled copper crucible. The ingots were melted five times and flipped for each melt to ensure the homogeneity of the alloy. The as-cast ingots were wire cut into 6 mm × 6 mm × 3 mm specimens, which were manually polished with SiC abrasive paper to 2000 grade and ultrasonically cleaned in ethanol for 10 min. The pack cementation mixture was composed of *Si* as the source material for coating, Al_2O_3 as the filler material, and NaF as the activating agent in a weight percent ratio of 30:65:5 [35,36]. The $AlMo_{0.5}NbTa_{0.5}TiZr$ specimens were sealed in an alumina crucible with the pack cementation powder mixture, where Al_2O_3 served as an anti-sintering agent and NaF served as an activator to prevent solid diffusion. The sealed crucible was bonded with ceramic slurry and placed into a tube furnace.

The pack cementation process was carried out in a continuous flow of Ar atmosphere (99.9 %) to prevent oxidation of the specimens at temperatures of 900 °C, 1000 °C, 1100 °C, and 1200 °C, with different coating times of 12, 24, and 48 h. The thickness of the coating layer was measured for each variation. The amounts of Si and NaF used in the process were varied to observe the effect on coating thickness, with Si ranging from 10 to 30 wt% and NaF from 1 to 5 wt%. The amount of Al_2O_3 was adjusted to maintain a weight ratio when reducing the amount of *Si* and NaF. The specimens coated with optimized thickness of silicide were selected for oxidation testing in an air atmosphere at 1300 °C for up to 100 h in a muffle furnace. The uncoated specimens were subjected to oxidation testing at the same temperature and time to enable comparison of oxidation results. The crystal structure and phases of oxidation products were determined using a Bruker D8 Advance X-ray diffractometer with CuKα radiation at room temperature within the 2θ range of 20–90° to the specimen surface. Additionally, the microstructure and cross-sectional analysis of the oxidation layer were characterized by a field emission scanning electron microscope (FE-SEM, Hitachi SU5000) equipped with backscattered electron (BSE) and energy dispersive spectrometer (EDS) detectors. The compositional information of the oxides layer at the cross-section of specimen, X-ray photoelectron spectroscopy (XPS) has been studied by using PHI 5000 VersaProbe (Ulvac-PHI) X-photoelectron spectrometer with monochromatized Al Kα excitation ($h\nu = 1486.6$ eV) operating at a pressure around 10^{-9} mbar.

3. Result and discussion

3.1. Phase composition and microstructure of $AlMo_{0.5}NbTa_{0.5}TiZr$

The X-ray diffraction spectra of the as-cast $AlMo_{0.5}NbTa_{0.5}TiZr$ alloy specimen is shown in Fig. 1(a). All the reflections in the XRD have been identified, and it has been confirmed that there are two main phases, *BCC* and *B2*, along with other impurity phase such as Al_2Zr_3. The calculated lattice parameters are 0.326 nm and 0.330 nm, respectively.

The microstructure of as-cast $AlMo_{0.5}NbTa_{0.5}TiZr$ alloy is shown in Fig. 1(b) and EDS analysis results are given in Table 1. The dendrite structure was observed and which is divided into bright and dark regions as shown in BSE image. The EDS analysis confirms the alloy was composed of *Al* 18.5 %, *Mo* 9.0 %, *Nb* 22.3 %, *Ta* 8.1 %, *Ti* 21.6 and *Zr*

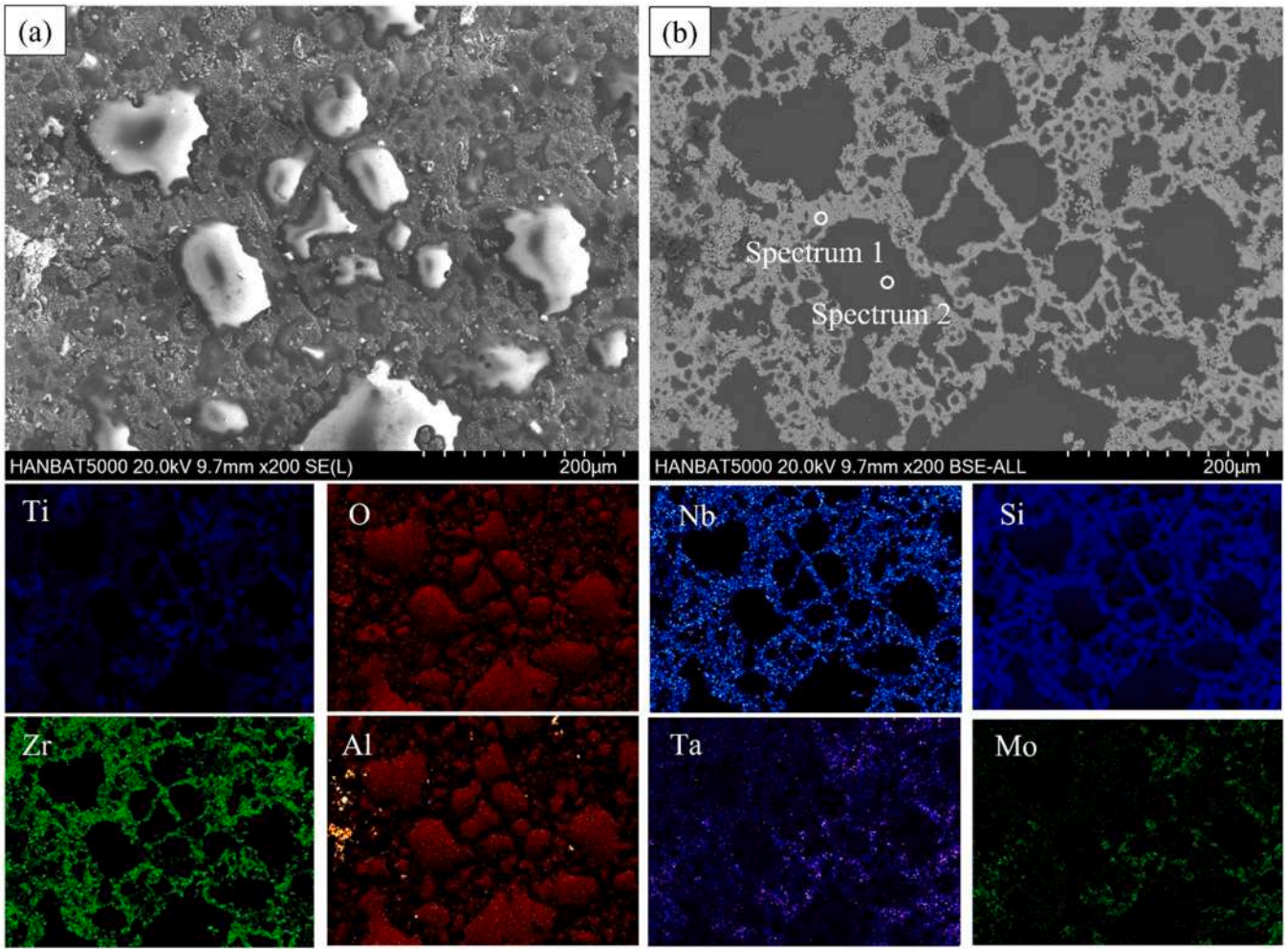

Fig. 2. (a) SEM image of surface (b) BSE image of Si coated $AlMo_{0.5}NbTa_{0.5}TiZr$ alloy at 1100 °C for 48 h and elemental mapping images.

Table 2
EDS data of *Si* coated specimen surface at 1100 °C for 48 h.

at%	*O*	*Al*	*Si*	*Ti*	*Zr*	*Nb*	*Mo*	*Ta*
1	17	1.2	55	8	7	6.3	3	2.5
2	63.7	15.2	20.8	0.1	0.1	–	–	–

20.2 %. In the magnified image, the bright region was examined as a region rich with *Mo*, *Nb*, and *Ta* elements which belongs to *BCC* phase, and the dark region was examined as a region rich with *Al, Ti*, and *Zr* which belongs to *B2* phase. Both of these phases have the characteristics of high-temperature stability and strength.

3.2. Coating characterization of $AlMo_{0.5}NbTa_{0.5}TiZr$

Fig. 2(a) shows the SEM of the Si coated surface of the $AlMo_{0.5}NbTa_{0.5}TiZr$ alloy at 1100 °C for 48 h. The surface exhibited irregularly shaped grains, indicating that the extent of coating was not the same for all constituents of the substrate. To determine the composition of the surface, BSE imaging was analyzed with EDS measurements and

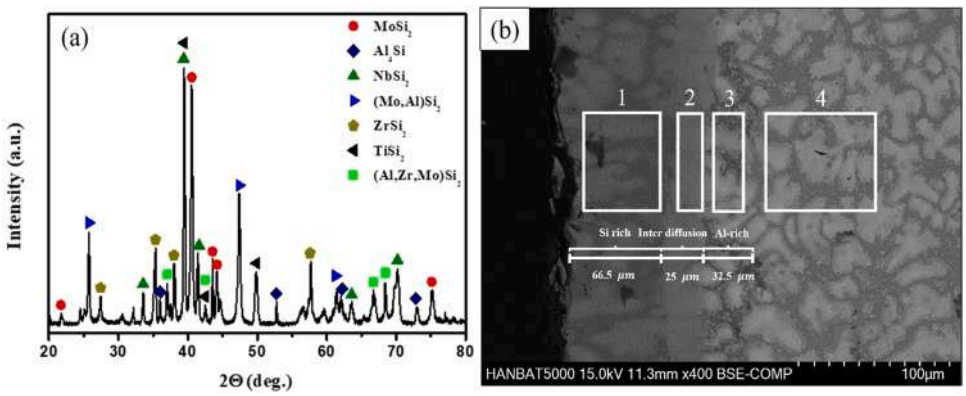

Fig. 3. (a) XRD pattern (b) BSE image of *Si* coated $AlMo_{0.5}NbTa_{0.5}TiZr$ alloy at 1100 °C for 48 h.

Table 3
EDS data of $AlMo_{0.5}NbTa_{0.5}TiZr$ specimen after 48 h silicide coatings at 1100 °C.

at%	*Al*	*Si*	*Ti*	*Zr*	*Nb*	*Mo*	*Ta*
1	–	70.2	9.0	–	9.5	5.1	5.9
2	1.2	68.3	7.1	–	10.0	6.8	6.4
3	50.5	–	8.7	22.1	11.9	–	6.6
4	16.9	–	20.5	21.5	21.4	10.1	9.4

elemental mapping. Fig. 2(b) illustrates the BSE and elemental mapping images of the surface of the specimen coated at 1100 °C for 48 h using Si pack cementation. A thick layer of Si formed on the surface due to the coatings, which suggests evidence of gas diffusion, and the composition of the surface was non-uniform. The detailed EDS analysis results are shown in Table 2. After gas diffusion due to Si pack cementation coatings, XRD and cross-sectional images were examined to observe the detailed phase formation.

The *Si*-rich layer confirmed on the surface of $AlMo_{0.5}NbTa_{0.5}TiZr$ alloy after pack cementation process and interdiffusion layer was observed next to the Si-rich layer. The x-ray diffraction pattern for silicide coated $AlMo_{0.5}NbTa_{0.5}TiZr$ alloy at 1100 °C for 48 h is shown in Fig. 3(a). All the reflections are corresponding to the complex silicide such as $NbSi_2$, Al_4Si, $MoSi_2$, $ZrSi_2$, (Al, Zr, Mo)Si_2, (Mo, Al)Si_2. Therefore, this coating layer is expected to improve oxidation resistance at high temperatures. Fig. 3(b) cross-sectional image of $AlMo_{0.5}NbTa_{0.5}TiZr$ alloy after coating at 1100 °C for 48 h. The cross-section image shows, silicon diffused into the specimen, and 4 distinct layers clearly seen such as *Si*-rich layer, inter-diffusion layer, *Al*-rich layer and specimen. The EDS analysis of these different layers is shown in Table 3, and the detailed analysis of the cross section is shown in Fig. 4 by performing elemental mapping analysis.

Fig. 4 shows cross-sectional magnified BSE image and elemental mapping images of *Si* coated $AlMo_{0.5}NbTa_{0.5}TiZr$ alloy at 1100 °C for 48 h. In the enlarged BSE image, the *Si*-rich layer, inter diffusion layer, and Al-rich layer observed in the coated specimen. Additionally, when

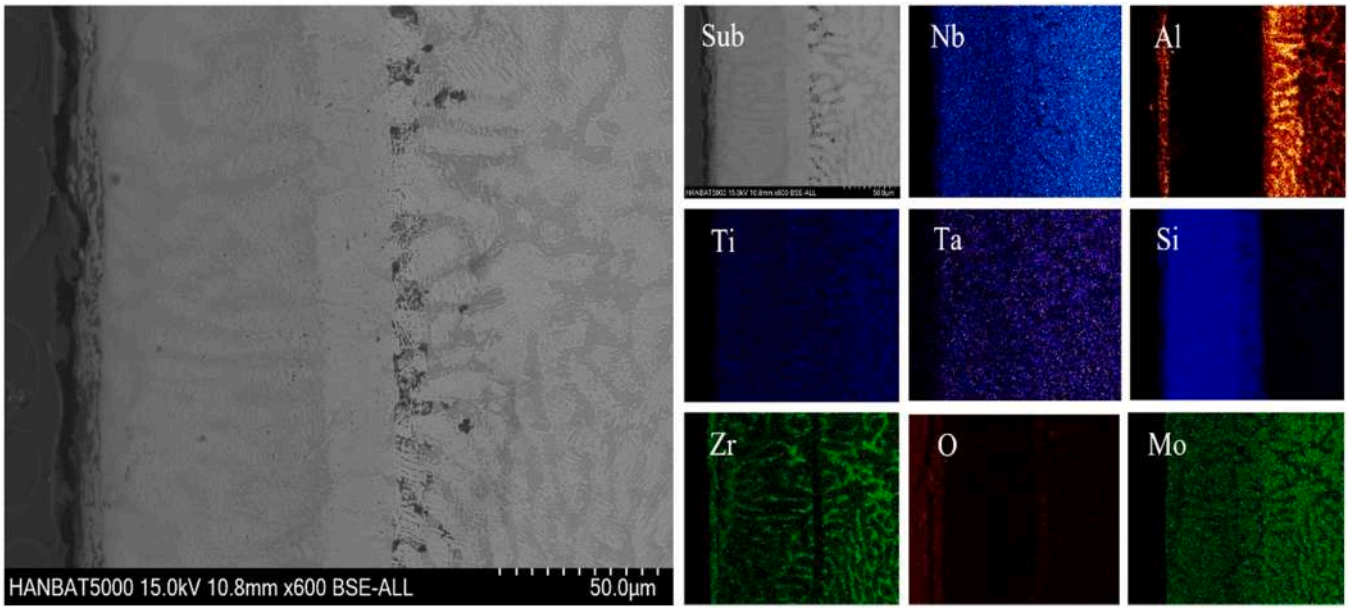

Fig. 4. Cross-sectional magnified BSE image and elemental mapping images of *Si* coated $AlMo_{0.5}NbTa_{0.5}TiZr$ alloy at 1100 °C for 48 h.

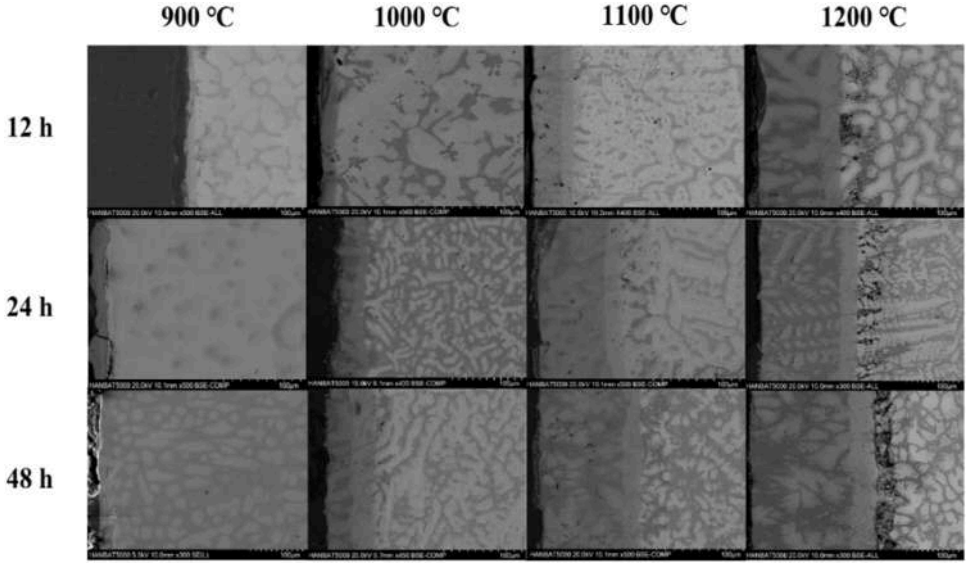

Fig. 5. Cross-section images of specimen at different time and temperature coating conditions.

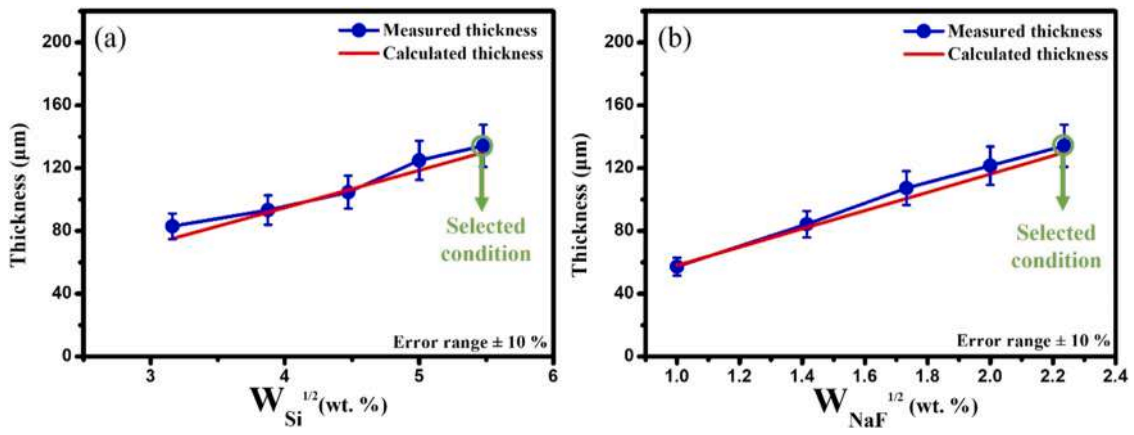

Fig. 6. Graph of coating layer thickness according to (a) *Si* and (b) *NaF* powder content inside the pack under the condition of 1100 °C 48 h.

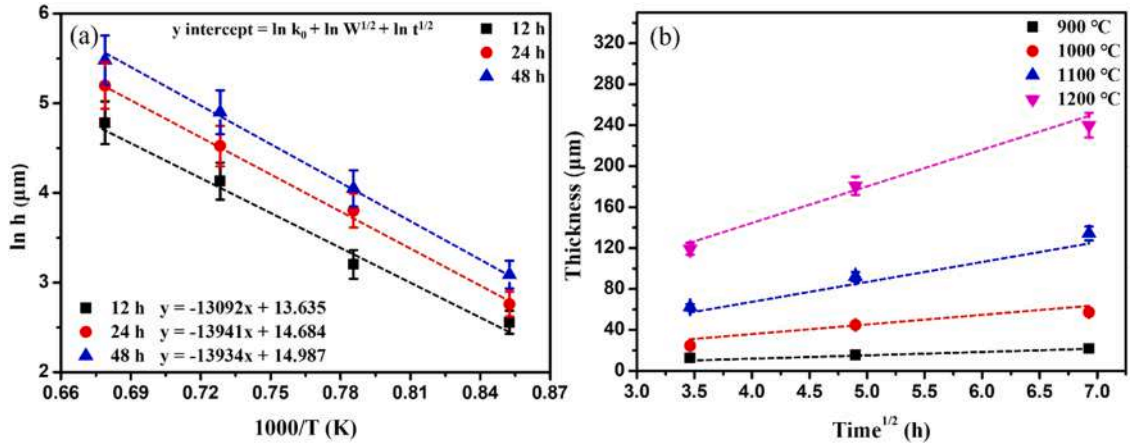

Fig. 7. (a) Change in *ln* h with respect to inverse of temperature and time and (b) Change in thickness of coating layer with respect to temperature and time.

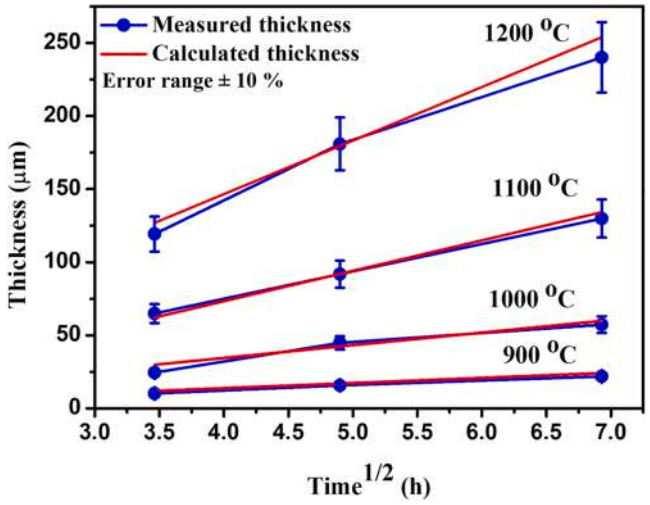

Fig. 8. Change in coating layer thickness with respect to heat treatment time at different temperature.

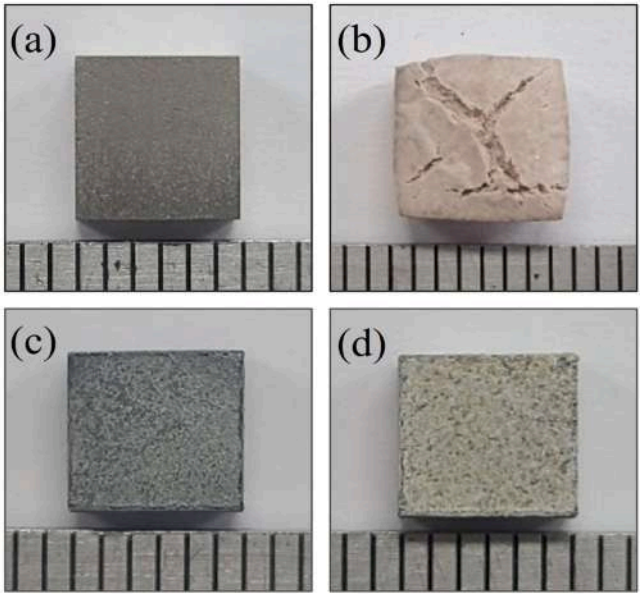

Fig. 9. Photos of $AlMo_{0.5}NbTa_{0.5}TiZr$ alloy (a) Un-coated specimen before oxidation, (b) Un-coated specimen after oxidation at 1300 °C for 10 h, (c) Silicide coated specimen before oxidation and (d) Silicide coated specimen after oxidation at 1300 °C for 60 h.

viewed from the elemental mapping analysis, the *Si*-rich layer formed due to the *Si* pack cementation coating, and the inter diffusion layer is also considered to be a layer formed by the reaction of the elements present inside and the diffused into the *Si*-rich layer. In addition, it is considered that the *Al*-rich layer is formed close to the inter diffusion

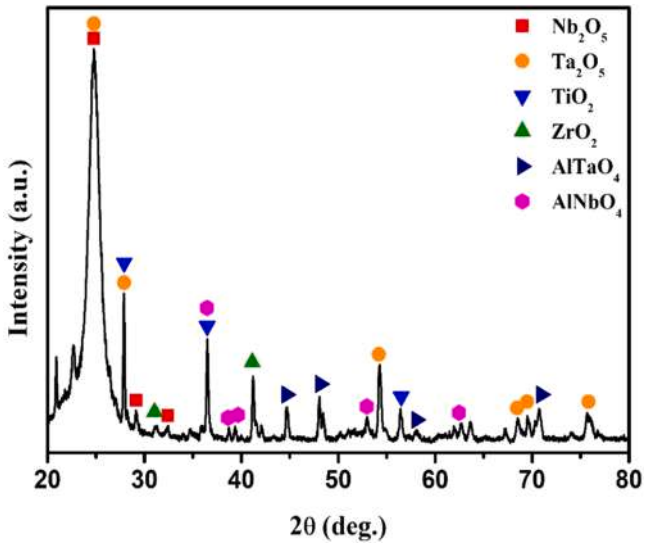

Fig. 10. XRD pattern of uncoated $AlMo_{0.5}NbTa_{0.5}TiZr$ alloy after oxidation test at 1300 °C for 10 h.

layer. Therefore, the change of the coating layer for each condition is shown in Fig. 5.

The cross-sectional images in Fig. 5 show the Si pack cementation coating at 900 °C, 1000 °C, 1100 °C and 1200 °C for 12 h, 24 h and 48 h. At a lower temperature of 900 °C, it is evident that the coating layer is unsatisfactory due to its thickness, adherence to the base material, and homogeneity. Additionally, by increasing the coating time under a coating temperature of 1000 °C did not result in a considerable increase in the thickness of the coating layer. Therefore, the coating temperature was increased, and a considerable thickness of coating layer was obtained. However, cracks were observed at the interface between the base material and the coating layer at a coating temperature of 1200 °C. Thus, it appears that the optimal coating condition is 1100 °C for 48 h, as this condition provides the best adhesion and stability of the base material.

Fig. 6 shows the variation in thickness of the silicide coating layer with respect to the weight percentage of Si and NaF at 1100 °C for 48 h. In Fig. 6(a), the Si powder content inside the pack was varied from 10 to 30 wt%. The thickness of the coating layer exhibited a linearly increasing trend as the Si powder content increased. It was observed that the amount of Si powder had a significant impact on the growth of the coating layer. Similarly, in Fig. 6(b), the NaF powder content was varied from 1 to 5 wt%, and the thickness of the coating layer increased linearly with an upward trend as the NaF content increased to 5 wt%.

3.3. Coating growth kinetics

The silicon coating on the $AlMo_{0.5}NbTa_{0.5}TiZr$ specimen by pack cementation is typically achieved by chemical vapor deposition, which is activated by salts of NaF halide. When temperature is high *Si* vapors migrated along with NaF vapors to the substrate surface started to deposit and diffused in to the substrate surface. The process and growth kinetics of the coating layer on the metallic substrate surface in pack cementation depend highly on the chemical composition and partial pressure of vapor species generated in the pack at high temperatures. In the diffusion-controlled growth process, the amount of coating layer deposited on surface of unit area at a time interval t (h) follows a parabolic law according to Levin et. al [34] and can be expressed as,

$$m^2 = k_g t \tag{1}$$

where, m is the weight gain (mg/cm^2), *kg* is the parabolic rate constant (mg^2 cm^4/s) and t is the coating time (s). The parabolic rate constant was given by following expression,

$$k_g = ((2n\varepsilon M_{Si} \Big/ IRT(\sum Di(pi - p'i))^{1/2} \tag{2}$$

where, n is the Si density in the pack, ε is the correction factor for pack porosity, M_{Si} is the atomic weight of *Si*, I is the correction factor for the pack pore length, R is the gas constant, and T is heat treatment temperature, Di is the diffusion rate of *Si* vapor, pi is the equilibrium partial pressure of the halide gas inside the pack, and pi' is the equilibrium partial pressure of the halide gas on the substrate surface. In this equation all the parameters except M_{Si} are constants and Eqs. (1) and (2) gives weight gain expression as follow,

$$m = k_p W_{Si}^{1/2} t^{1/2} \tag{3}$$

where, k_p is the rate constant at coating temperature (mg^{2}cm^4/s), W_{Si} is the Si content [wt%] and t is the coating time (s). In terms of how much activator was employed in pack cementation, the coating kinetic equations proposed by Xiang et al. [34] do not accurately predict the development of the coating layer. Therefore, a factor which depends on the amount of activator was introduced and the equation was modified as follows,

$$m = k_p W_{Si}^{1/2} t^{1/2} (A/5)^{1/2} [(A/5)^{1/2} = 1] \tag{4}$$

where, A is the NaF content [wt%] inside the pack. Fig. 6(b) shows the growth of the coating layer according to the NaF content by using Eq. (4). The modified Eq. (4) shows that if there is no loss of the deposition element and the deposition area is converted to the Silicide. The relationship between the amount of Si deposited on substrate or the weight gain (m) and the coating thickness in μm (h) can be given by,

$$h = m10M_c/(yM_{Si}\rho) \tag{5}$$

where, M_C is the molecular weight of the formed intermetallic compound [g/mol], and ρ is the density of the formed coating layer [g/cm^3]. The Eqs. (4) and (5) gives,

$$h = k_s W^{1/2} t^{1/2} (A/5)^{1/2} \tag{6}$$

where k_s is a rate constant of halide gas at constant temperature. The above formula represents the diffusion coefficient when coating the intermetallic compound and temperature dependance. The relationship between diffusion coefficient and activation energy can be expressed according to the Arrhenius formula,

$$k_s = k_0 \quad \exp(-Q/RT) \tag{7}$$

where, Q is the activation energy [kJ/mol] required for the growth of the coating layer, R is the gas constant, T is the coating temperature (°C), and k_0 is the rate constant. Substituting Eq. (7) into Eq. (6) we get an expression as,

$$h = k_0 W^{1/2} t^{1/2} (A/5)^{1/2} \quad \exp(-Q \Big/ RT) \tag{8}$$

The rate constant coefficient k_0 can be determined from the experimental results after taking the natural logarithm of both sides equation and fitting with experimental results.

$$\ln \quad h = \ln \quad k_0{}^{1/2} + \ln \quad W^{1/2} + \ln \quad t^{1/2} + \ln((A/5)^{1/2}) - Q \Big/ RT \tag{9}$$

The optimized value of NaF is 5 wt% in pack cementation process, hence $(A/5)^{1/2} = 1$, so the Eq. (9) becomes,

$$lnh = \ln \quad k_0{}^{1/2} + \ln \quad W^{1/2} + \ln \quad t^{1/2} - Q/RT \tag{10}$$

Fig. 7(a) shows the linear relationship between ln h and 1000/T according to the coating temperature and time. The slope of each graph is Q/R, and the activation energy Q can be calculated from the average slope value. The average value of activation energy under the conditions

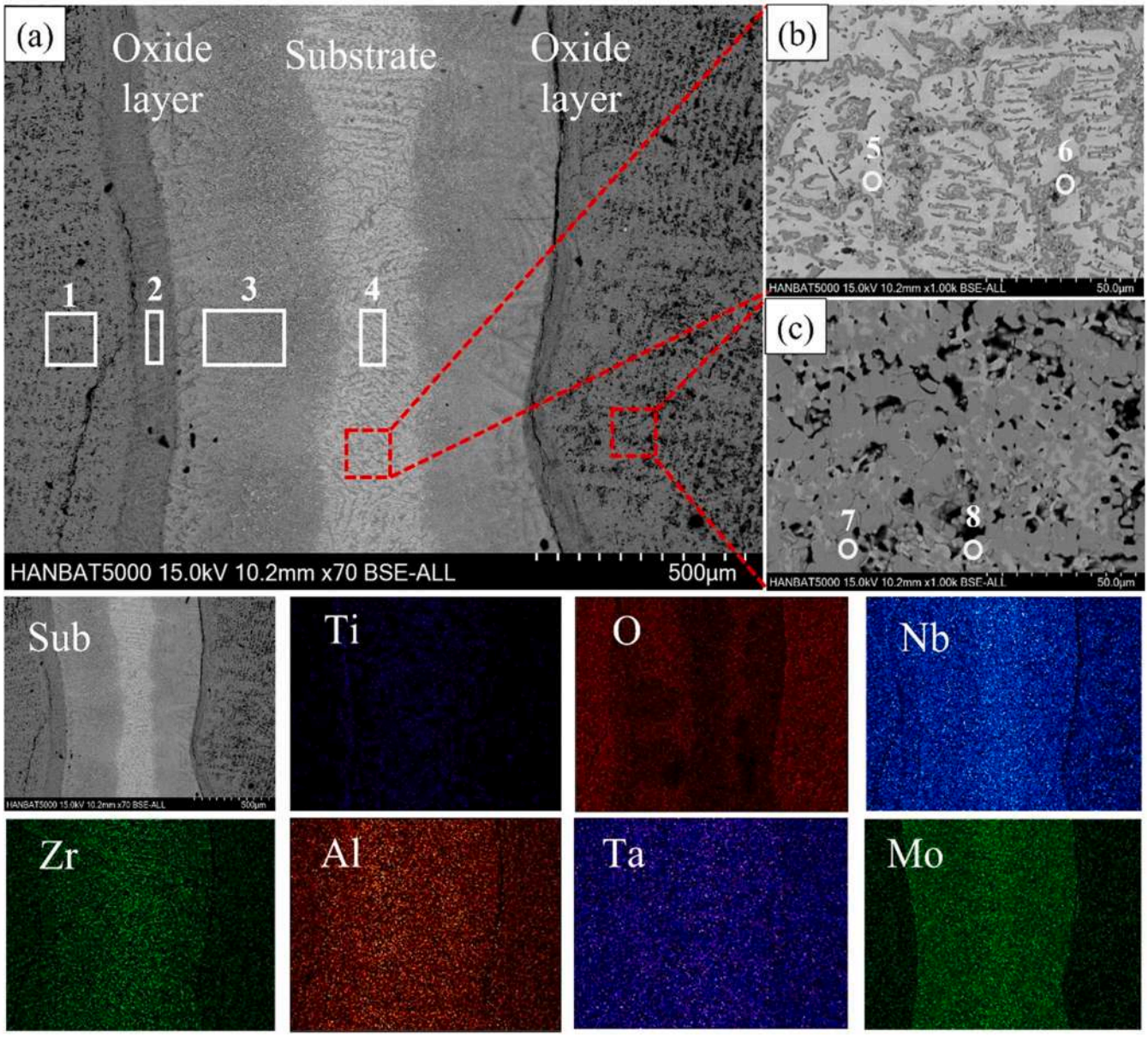

Fig. 11. The SEM image of cross-sectional view, BSE and elemental mapping images of uncoated $AlMo_{0.5}NbTa_{0.5}TiZr$ alloy after oxidation test at 1300 °C for 10 h.

Table 4
EDS compositional analysis of different areas of uncoated specimen after oxidation at 1300 °C 10 h.

at%	*O*	*Al*	*Ti*	*Zr*	*Nb*	*Mo*	*Ta*
1	71.7	5.8	5.8	6.7	6.5	–	3.1
2	64.7	8.1	6.8	9.2	7.6	–	3.6
3	59.6	9.1	7	10.4	7.0	3.4	3.4
4	41.0	10	11.2	15.4	11.4	5.7	5.3
5	14.2	23.4	15.5	3.2	22.0	10.6	11.1
6	52.6	5.3	3.6	27.5	6.4	2.6	2.0
7	71.1	2.0	4.8	2.6	14.2	–	5.3
8	70.8	6.4	6.0	9.6	5.2	–	2.6

of 12 h, 24 h and 48 h was $Q = 117$ kJ/mol. In addition, the k_0 value for each coating time can be obtained from the y-intercept of Fig. 7(a), and the average k_0 *(1)* from 12 h to 48 h was calculated to be 94,497 μm/h$^{1/2}$. The change in coating layer thickness with respect to different coating temperature and time is shown Fig. 7(b). The Eq. (8) can be re-written as,

$$h \Big/ t^{1/2} = k_0 W_{si}^{1/2} \exp(-Q \Big/ RT) \tag{11}$$

The value of k_0 *(2)* calculated from the slope value of Fig. 7(b), and the derived average value of k_0 *(2)* was 101,199 μm/h$^{1/2}$. When we re-arranged Eq. (8) according to the thickness of the coating layer and the Si content.

$$h \Big/ W_{Si}^{1/2} = k_0 t^{1/2} \exp(-Q \Big/ RT) \tag{12}$$

The value of k_0 *(3)* calculated from the slope value of Fig. 8. The k_o (3) derived value was 94,774 μm/h$^{1/2}$. Therefore, the average values of k_0 *(1)*, k_0 *(2)* and k_0 *(3)* were used in the final equation as k_0 = 96,823 μm/h$^{1/2}$ and substituting into Eq. (8),

$$h = 96823 W_{Si}^{1/2} \quad t^{1/2} \exp(-117 \Big/ T) \tag{13}$$

To confirm the usefulness of Eq. (13) in our study, the experimental results were compared with calculated results as shown Fig. 8.

The change in the silicide coating-layer thickness on

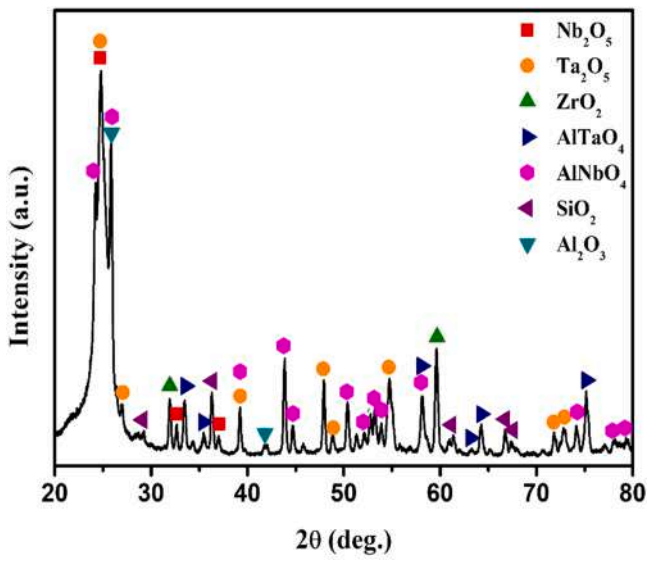

Fig. 12. XRD pattern of coated $AlMo_{0.5}NbTa_{0.5}TiZr$ alloy after oxidation test at 1300 °C for 100 h.

$AlMo_{0.5}NbTa_{0.5}TiZr$ alloy with respect to the heat treatment time at different temperature at 30 wt% of Si and 5 wt% of NaF is shown in Fig. 8. The silicide coating were carried out at different temperatures 900 °C, 1000 °C, 1100 °C, and 1200 °C for 12 h, 24 h, and 48 h. The measured thickness was compared with the calculated thickness by using Eq. (13) and it is observed that linear relationship between coating thickness and time. For all specimens coated with 30 wt% *Si* and 5 wt% NaF, an error of 5.5 % was obtained when the error was calculated during coating at 900–1200 °C for 12–48 h. Also, the errors according to the *Si* content and NaF content were 4.5 % and 3.9 %, respectively, as shown in Fig. 8. Therefore, Eq. (13) is considered to be a good reference for coating layer thickness modulation for the $AlMo_{0.5}NbTa_{0.5}TiZr$ alloy. In order to measure the oxidation resistance of the optimized coating layer condition of specimen, an oxidation experiment was performed at 1300° for up to 100 h.

3.4. Oxidation behaviors

To study the oxidation resistance of *Si* pack cementation on $AlMo_{0.5}NbTa_{0.5}TiZr$ alloy, an isothermal oxidation test in open air were carried out. Fig. 9 shows the appearance images of $AlMo_{0.5}NbTa_{0.5}TiZr$ alloy specimen (a) before coating (b) after oxidation at 1300 °C for 10 h, (c) silicide coated specimen and (d) silicide coated specimen after oxidation at 1300 °C for 60 h. it can be seen that the $AlMo_{0.5}NbTa_{0.5}TiZr$ alloy was oxidized under high temperature conditions to form cracks and the appearance of the specimen swelled and deformed from its original shape. However, after coating as shown in Fig. 9(d), the appearance of the shape of specimen was maintained even under the same oxidizing condition, and deformation such as cracks or expansion was not observed in the specimen but color become dark gray.

As shown in Fig. 10, the diffraction peaks of the *BCC* and *B2* phase of original specimen $AlMo_{0.5}NbTa_{0.5}TiZr$ can no longer be seen, indicating that the alloy substrate has formed a thicker oxide layer on the surface after being oxidized at 1300 °C for 10 h. It is observed that the oxidation products consist of complex of oxides of Nb_2O_5 (ICDD: 00-009-0372), Ta_2O_5 (ICDD: 01-073-2323), TiO_2 (ICDD: 01-088-1175), ZrO_2 (ICDD: 00-001-0750), $AlTaO_4$ (ICDD: 00-041-0347), and $AlNbO_4$ (ICDD: 00-025-1490). Surprisingly, we observed that there is no any traces of MoO_3 formation due to the reason that at higher temperatures molybdenum oxides are volatile. To verify the elemental distribution of *Al, Mo, Nb, Ta, Ti, Zr*, and *O* elemental mapping were carried out and Fig. 11 (a) shows the results of cross-sectional SEM and elemental mapping images of uncoated $AlMo_{0.5}NbTa_{0.5}TiZr$ alloy after oxidized in air at 1300 °C for 10 h. At this condition, specimen losses its shape due to extreme oxidation and cross-section view at the middle part of specimen. The higher magnification images from white region and black region shown in Fig. 11 (b, c). The EDS analysis distinguish specimen layer and oxides layers which is given in Table 4. It is seen that oxygen contents decreases

Table 5
EDS data *Si*-coated $AlMo_{0.5}NbTa_{0.5}TiZr$ specimen after oxidation at 1300 °C for 20 h.

at%	*O*	*Al*	*Si*	*Ti*	*Zr*	*Nb*	*Mo*	*Ta*
1	71.6	19.3	8.9	0.2	–	–	–	–
2	72.4	1.6	23.4	0.6	2.0	–	–	–

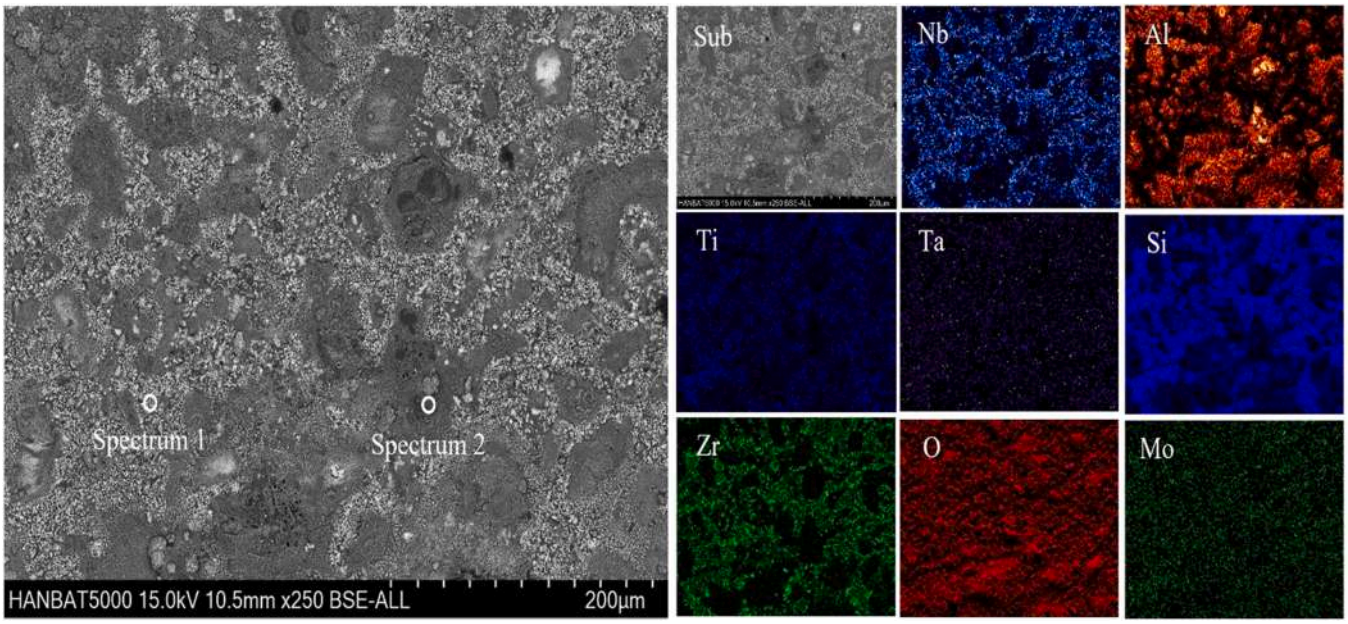

Fig. 13. Surface BSE image and elemental mapping images of *Si*-coated specimen after oxidation at 1300 °C for 20 h.

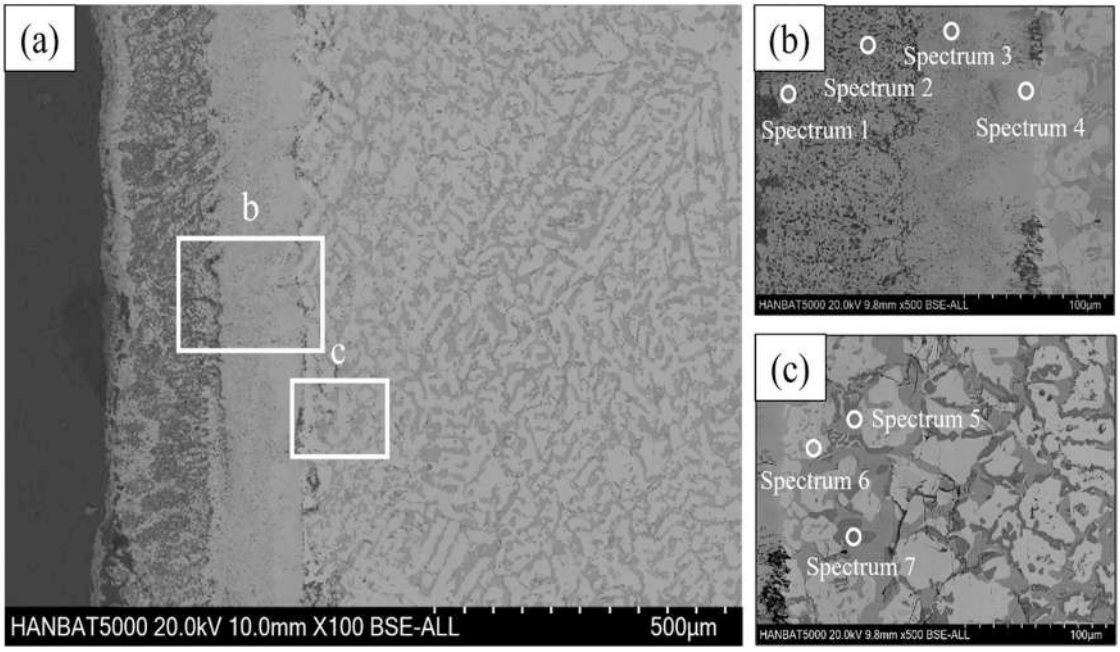

Fig. 14. Cross-sectional BSE image of *Si*-coated specimen after oxidation at 1300 °C for 100 h.

Table 6
EDS compositional analysis of Si-coated $AlMo_{0.5}NbTa_{0.5}TiZr$ specimen after oxidation at 1300 °C 100 h.

at%	*O*	*Al*	*Si*	*Ti*	*Zr*	*Nb*	*Mo*	*Ta*
1	64.3	0.1	18.5	1.3	11.8	2.1	1.1	0.8
2	28.6	0.1	35.4	2.6	16.3	9.0	5.6	2.3
3	53.0	0.2	20.1	2.1	16.5	4.8	1.9	1.4
4	8.5	2.0	38.4	12.1	17.6	12.7	4.2	4.6
5	–	36.7	2.3	12.7	29.3	11.1	5.1	2.7
6	–	32.7	–	13.2	4.3	24.4	13.3	12.1
7	–	52.8	1.0	5.9	28.9	6.3	4.4	0.8

from oxide layer to substrate due to diffusion of oxygen into the specimen. The elemental mapping analysis shows how oxygen penetrated in to the $AlMo_{0.5}NbTa_{0.5}TiZr$ alloy, *Mo* and *Zr* elements remained near the substrate while *Nb*, *Al*, *Ti*, and Ta elements were evenly distributed in the oxide layer. The complex oxide layers were formed due to the weak oxidation resistance, so it is difficult to use $AlMo_{0.5}NbTa_{0.5}TiZr$ alloy at high temperatures.

The XRD pattern of silicide coated $AlMo_{0.5}NbTa_{0.5}TiZr$ alloy specimen after oxidation at 1300 °C for 100 h is shown in Fig. 12. It is clearly seen that from microstructural and XRD analysis upper most layer consists of SiO_2 (00-001-0438) and Al_2O_3 (ICDD: 00-089-3072), oxides as well as Nb_2O_5 (ICDD: 00-009-0372), Ta_2O_5 (ICDD: 01-073-2323), ZrO_2 (ICDD: 00-001-0750), $AlTaO_4$ (ICDD: 00-041-0347), and $AlNbO_4$ (ICDD: 00-025-1490) phases of different oxides. The SiO_2 and Al_2O_3 protect the specimen from the further oxidation which is not observed in uncoated specimen of $AlMo_{0.5}NbTa_{0.5}TiZr$ alloy.

Fig. 13 is the surface BSE image and elemental mapping images of Si-coated specimen after oxidation at 1300 °C for 20 h. Based on the elemental mapping analysis, it is seen that SiO_2 formed on the surface of specimen due to oxidation and Al_2O_3 observed which is believed from the Al_2O_3 powder used in pack cementation. When the surface was analyzed by EDS, the larger amount of Al observed in Spectrum-1 and *Si* amount found to be larger in Spectrum-2. It is believed that the protective coating layers consists of SiO_2 and Al_2O_3, which protect the specimen at high temperature oxidizing environment. The EDS analysis results are shown in Table 5, and the cross-sectional image analysis of the specimen is shown in Fig. 14 for further analysis.

Fig. 14 shows BSE images of Si-coated specimens after oxidation at 1300 °C for 100 h. The silicide layer and an aluminide layer were formed on the surface of the specimen due to the silicide coating. It is considered that the rigid SiO_2 layers was formed on the surface through the diffusion under the high temperature oxidation conditions at 1300 °C for 100 h, whereas *Si*-rich layer, inter diffusion layer, and *Al*-rich layer, which were formed during the silicon coatings. And, the *Si* and *Al* contents in the coating layer were decreased, and the reduction of the *Si*-rich layer, inter diffusion layer and the *Al*-rich layer was confirmed in the mapping analysis. Also, the diffusion of *Al* in the interdiffusion layer was confirmed. The EDS analysis results confirms the high-temperature oxidation occurred with the *Si*-rich layer, the inter-diffusion layer, and the *Al*-rich layer, and which improved oxidation resistance under these conditions, so that the specimen was not oxidized and maintained its original shape. The EDS analysis results of the specimen is shown in Table 6.

The cross-sectional elemental mapping images of a *Si* coated specimen after 100 h of oxidation at 1300 °C were shown in Fig. 15. The image shows that oxides were formed at the surface, and a silicon-rich oxide was observed. The presence of silicon-rich oxide protected the coated alloy compared to the uncoated alloy specimen. Furthermore, an aluminum rich layer was observed adjacent to the substrate which is attributed to coming out Al from the surface of substrate alloy. However, aluminum was detected at the surface, which could be recognized to the presence of alumina powder [37].

The cross-section of the silicide-coated $AlMo_{0.5}NbTa_{0.5}TiZr$ alloy specimen was analyzed after oxidation at 1300 °C for 100 h to determine the different phases formed, as shown in Fig. 16. It is quite evident that the B2 and BCC phases are dominant in the specimen, as confirmed by the XRD peaks. This is because the specimen was exposed to the x-ray beam during the analysis. The presence of SiO_2, MoO_3, and ZrO_2 phases suggests that the oxidation of the specimen occurred at the surface. The Si-rich layer, which was observed to be larger than any other layer, could be attributed to the silicon coating process. The XRD peaks from $NbSi_2$ and $MoSi_2$ belong to the interdiffusion layer formed during the silicon coating process could be attributed to the reaction between the silicon coating and the underlying alloy substrate.

The cross-sectional line EDS analysis of the silicide-coated $AlMo_{0.5}NbTa_{0.5}TiZr$ alloy specimen after oxidation at 1300 °C for

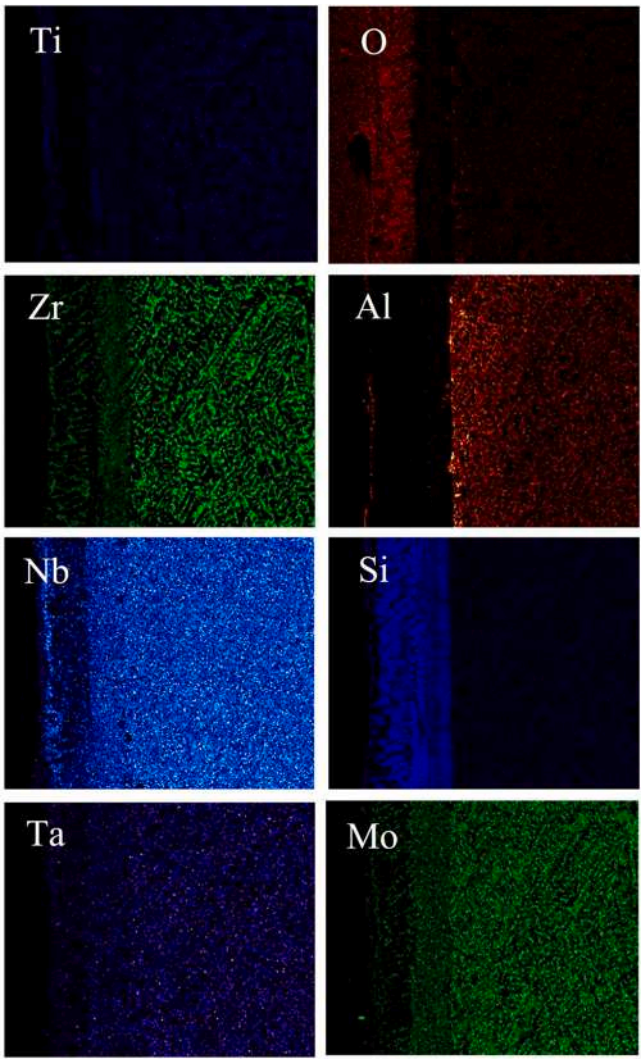

Fig. 15. Cross-sectional elemental mapping image of *Si*-coated specimen after oxidation at 1300 °C for 100 h.

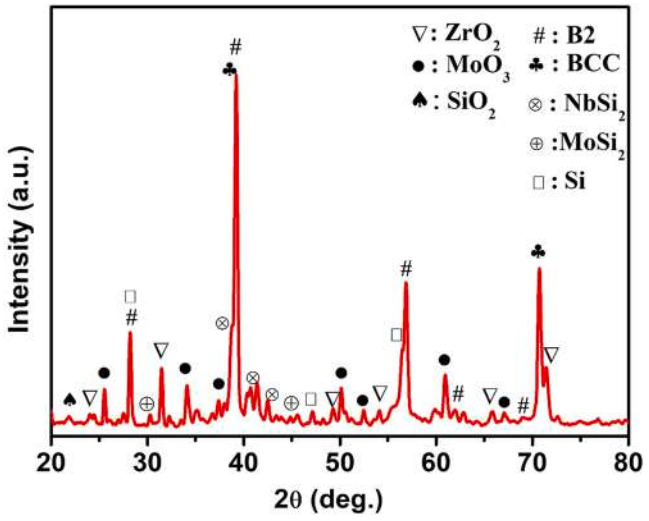

Fig. 16. Cross-sectional XRD pattern of Si coated $AlMo_{0.5}NbTa_{0.5}TiZr$ alloy after oxidation test at 1300 °C for 100 h.

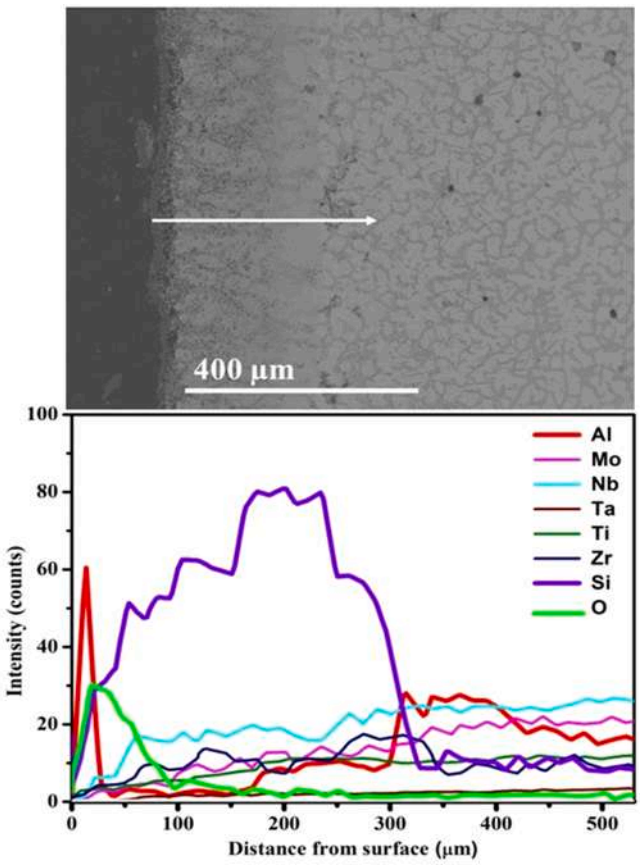

Fig. 17. Cross-sectional line EDS profile of Si coated $AlMo_{0.5}NbTa_{0.5}TiZr$ alloy after oxidation test at 1300 °C for 100 h.

100 h is presented in Fig. 17. The line EDS was measured from the outer side of the specimen to the inner side. In the cross-sectional images, different layers were observed within 0–400 μm distance from the surface of the specimen. The line EDS analysis indicates that the elemental concentrations were rather constant after 400 μm, but the concentration of elements such as Si, Al, and O varied within 400 μm due to silicon coating and oxidation at 1300 °C. During the silicon coating process, Si diffusion occurred at the interface with the specimen, and Zr, Mo, and Al elements from the surface of the specimen diffused into the Si layer. Interestingly, the Al element was trapped just under the Si layer, resulting in a higher concentration of Al at 300–350 μm. The Aluminium was also observed at the surface, which may have been from the Al_2O_3 powder used during the pack cementation process. The concentration of oxygen was higher at the surface and decreased from the outer to the inner side, suggesting that the coating process was used to protect the $AlMo_{0.5}NbTa_{0.5}TiZr$ alloy from oxidation.

The x-ray photoemission spectroscopy (XPS) technique is used to understand the chemical oxidation states and the ligand coordination of $AlMo_{0.5}NbTa_{0.5}TiZr$ alloy specimen. The high resolution XPS spectra with deconvoluted peaks using XPSpeakfit41 software with an iterative Shirley-type background subtraction for Si, Mo, O, Zr, Nb, Al, Ti, and Ta given in Fig. 18. The deconvoluted XPS spectra for Si $2p_{3/2}$ shows two different peaks at binding energies 98.4 eV and 102.3 eV which are corresponding to Si and SiO_2 [37,38]. Similarly, XPS spectra for Al $2p_{3/2}$ shows two distinct peaks at 71.3 eV and 74.1 eV which confirms the presence of metallic Al and Al_2O_3, respectively [39]. However, Zr $3d_{5/2}$, Nb $3d_{5/2}$, Ti, $2p_{1/2}$, Ta $4d_{3/2}$, and Mo $3d_{5/2}$ spectra shows the oxidation state of respective elements into the specimen.

The mass increase of an uncoated and coated $AlMo_{0.5}NbTa_{0.5}TiZr$ specimens with different oxidation times is shown in Fig. 19. Inset of figure shows mass gain for uncoated specimen for 10 h oxidation time.

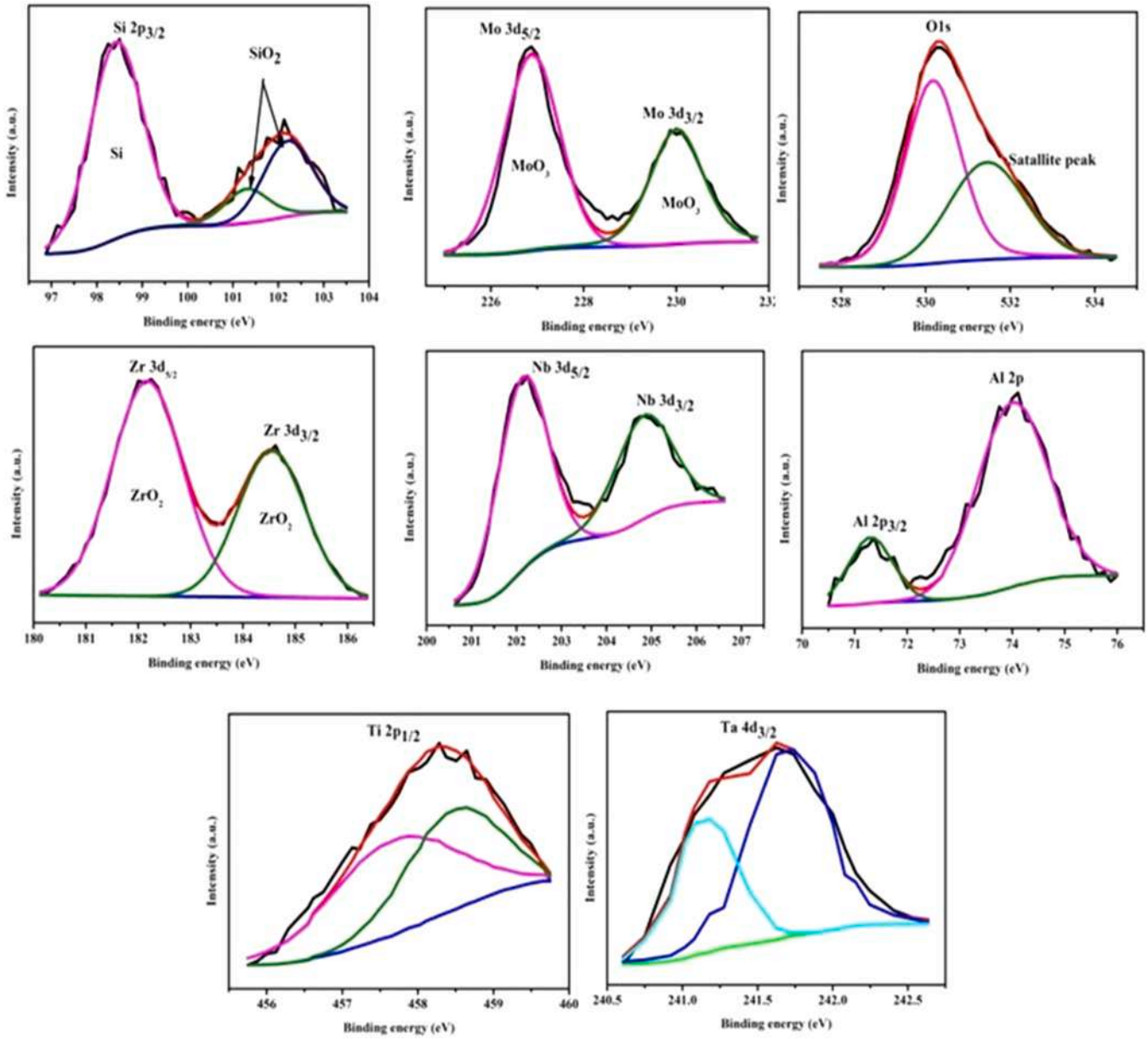

Fig. 18. High-resolution XPS spectra of Si 2p, Mo 3d, O 1 s, Zr 3d, Nb 3d, Al 2p, Ti 2p and Ta 4d for cross-sectional XPS of Si coated $AlMo_{0.5}NbTa_{0.5}TiZr$ specimen after oxidation at 1300 °C.

The weight gain per unit area due to oxidation was 16,818 mg^2/cm^4, whereas the coated specimen showed weight gain of 60 mg^2/cm^4, 183 mg^2/cm^4, 439 mg^2/cm^4, 647 mg^2/cm^4, and 710 mg^2/cm^4, respectively. It is seen that as the oxidation time increased, the weight increase per unit area increased, but the difference in the amount of mass gain change was smaller than the uncoated specimen. These results confirms that *Si* coated $AlMo_{0.5}NbTa_{0.5}TiZr$ specimen improves oxidation resistance at high temperature and thus its use for different application at elevated temperature.

The schematic representation of the $AlMo_{0.5}NbTa_{0.5}TiZr$ alloy specimens, including as-cast, after oxidation test, silicide-coated, and silicide-coated after oxidation, are shown in Fig. 20 (a-d). The as-cast specimen exhibited weak oxidation resistance when exposed to high temperatures, and a thick oxide layer was clearly visible. In the silicide-coated specimen, different layers were formed on the alloy, including a *Si*-rich layer, an interdiffusion layer, and an *Al*-rich layer that emerged from the specimen. The formed coating layer is expected to act as a protective layer at high temperatures after the oxidation experiment. The SiO_2 rigid layer formed as a result of the oxidation of *Si* component from the specimen, at 1300 °C. However, the Al_2O_3 is probable to form from the alumina powder, and solutioned with SiO_2, resulting to form aluminosilicate [40]. The cross-sectional XRD, line EDS, elemental mapping, and XPS results support the different layers proposed in the schematic figure. The formed SiO_2 rich oxides protective layers which plays an important role in protecting the $AlMo_{0.5}NbTa_{0.5}TiZr$ alloy specimen at high temperature.

4. Conclusions

In summary, a novel refractory high entropy alloy, $AlMo_{0.5}NbTa_{0.5}TiZr$, was successfully prepared using arc melting and silicon coatings via the pack cementation method for the first time. By increasing the coating time at 1100 °C produced a silicide coating layer with good adherence on the $AlMo_{0.5}NbTa_{0.5}TiZr$ substrate and adequate thickness. Structural analysis confirmed the formation of $AlMo_{0.5}NbTa_{0.5}TiZr$, silicide layer formation after pack cementation, and complex oxides,

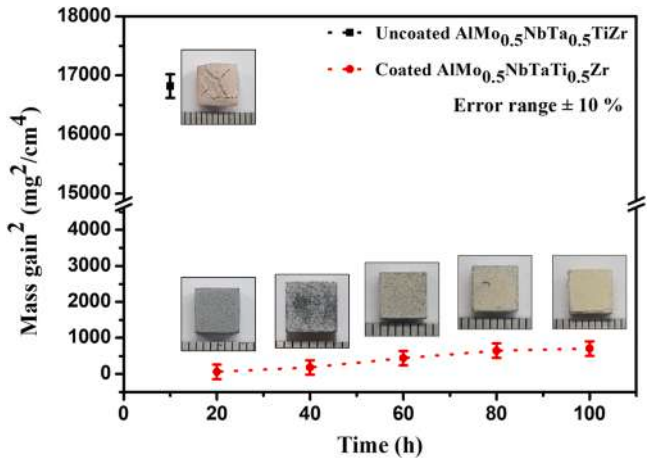

Fig. 19. Graph of mass gain of uncoated and coated $AlMo_{0.5}NbTa_{0.5}TiZr$ specimen with different oxidation time.

including $AlNbO_4$, TiO_2, SiO_2, Al_2O_3, and NbO_2, after oxidation testing at 1300 °C for varying time periods. When analyzing the growth kinetics of the coating layer, the amount of coating element Si as a source and NaF as an activator inside the pack cementation, as well as the coating temperature and time, were considered. The optimized amounts of *Si* and NaF were found to be 30 wt% and 5 wt%, respectively, with 65 wt% Al_2O_3 for all experiments. This is a condition to obtain a suitable coating layer, and even if the weight ratio of $Si:Al_2O_3:NaF$ is not necessarily 30:65:5, a coating layer with the same thickness can be obtained by adjusting the time and temperature. The coating temperature range was between 900 and 1200 °C, and the estimated average growth constant coefficient (*k0*) and activation energy (*Q*) were 96,823 μm/$h^{1/2}$ and 117 kJ/mol, respectively. The coating condition was optimized for temperature and time at 1100 °C and 48 h, resulting in the best coating layer thickness. The mathematical equations were used to determine the coating layer thickness based on variables such as temperature and time, and the values derived from calculation and experimentation were almost identical. The EDS analysis revealed a bright region containing oxides rich in *Mo, Nb*, and *Ta*, corresponding to the *BCC* phase, and a dark region containing oxides rich in *Al, Ti*, and *Zr*, corresponding to the *B2* phase. The comparison between coated and uncoated specimens gives an idea of the usefulness of silicon coatings on the $AlMo_{0.5}NbTa_{0.5}TiZr$ alloy. The cross-sectional XRD, elemental mapping, line EDS, and XPS analysis confirms the different layers formed during coating and oxidation process. The mathematical equations used in this study to understand coating layer growth kinetics can provide guidelines when selecting coating parameters. Therefore, it is believed that the $AlMo_{0.5}NbTa_{0.5}TiZr$ refractory high entropy alloy coated with silicon by the pack cementation method will be useful at 1300 °C.

CRediT authorship contribution statement

C. Hwang: Investigation, Validation, Writing – original draft. **K.P. Shinde:** Conceptualization, Writing – review & editing. **J. Oh:** Investigation, Formal analysis. **S. Lee:** Writing – review & editing. **C.H. Chung:** Writing – review & editing. **J.S. Park:** Conceptualization, Writing – review & editing, Supervision.

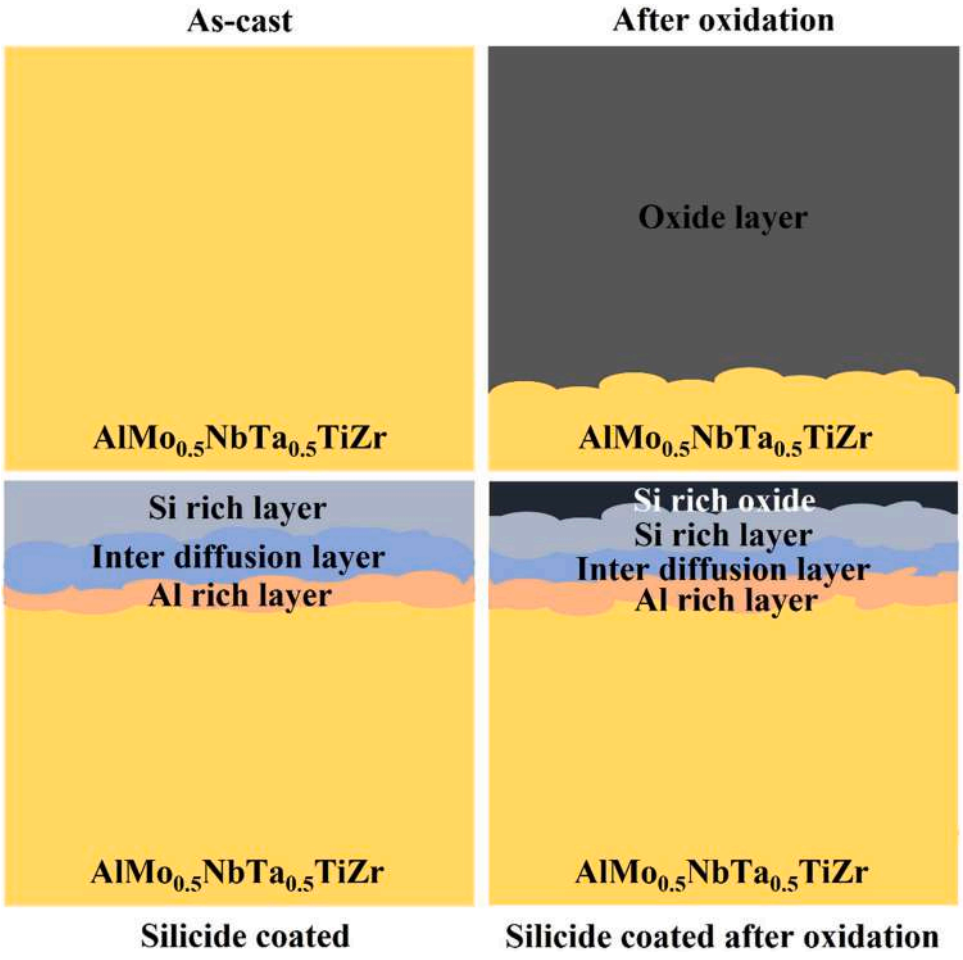

Fig. 20. Schematic image of $AlMo_{0.5}NbTa_{0.5}TiZr$ alloy (a) as-cast, (b) oxidation test, (c) silicide coated and (d) oxidation test after coating.

Declaration of Competing Interest

The authors declare that they have no known competing financial interests or personal relationships that could have appeared to influence the work reported in this paper.

Data Availability

Data will be made available on request.

Acknowledgement

This research was supported by National Research Foundation of Korea (NRF) funded by the Ministry of Education, Science and Technology (No. 2020R111A3070554) and "Regional Innovation Strategy (RIS)" through the National Foundation of Korea (NRF) funded by the Ministry of Education (MOE) (2021RIS-004) and Korea Institute for Advancement of Technology (KIAT) grant, funded by Republic of Korea Ministry of Trade, Industry and Energy (MOTIE) (P0002019, Human Resource Development Program for Industrial Innovation).

Author statement

I declare that the article is original, and all authors are aware of its content and approve its submission. Also, the article has not been published previously, and the article is not under consideration for publication elsewhere.

References

[1] D.B. Miracle, O.N. Senkov, A critical review of high entropy alloys and related concepts, Acta Mater. 122 (2017) 448, https://doi.org/10.1016/j.actamat.2016.08.081.
[2] Y. Tao, W. Houqin, K. Han, B. Zhang, Microstructure and wear behavior of AlCrTiNbMo high-entropy alloy coating prepared by electron beam cladding on Ti600 substrate, Vacuum 199 (2022), 110928, https://doi.org/10.1016/j.vacuum.2022.110928.
[3] J.W. Yeh, S.K. Chen, S.J. Lin, J.Y. Gan, T.S. Chin, T.T. Shum, C.H. Tsau, S.Y. Chang, Nanostructured high-entropy alloys with multiple principal elements: novel alloy design concepts and outcomes, Adv. Eng. Mater. 6 (2004) 299, https://doi.org/10.1002/adem.200300567.
[4] E.P. George, D. Raabe, R.O. Ritchie, High-entropy alloys, Nat. Rev. Mater. 4 (2019) 515, https://doi.org/10.1038/s41578-019-0121-4.
[5] S. Gorsse, D.B. Miracle, O.N. Senkov, Mapping the world of complex concentrated alloys, J. Acta Mater. 135 (2017) 177, https://doi.org/10.1016/j.actamat.2017.06.027.
[6] O.N. Senkov, D.B. Miracle, K.J. Chaput, J.P. Couzinie, Development and exploration of refractory high entropy alloys, J. Mater. Res. 33 (2018) 3092, https://doi.org/10.1557/jmr.2018.153.
[7] Y. Zhang, T.T. Zuo, Z. Tang, M.C. Gao, K.A. Dahmen, P.K. Liaw, Z.P. Lu, Microstructures and properties of high-entropy alloys, Prog. Mater. Sci. 61 (2014) 1, https://doi.org/10.1016/j.pmatsci.2013.10.001.
[8] O.N. Senkov, S. Gorsse, D.B. Miracle, High temperature strength of refractory complex concentrated alloys, Acta Mater. 175 (2019) 394, https://doi.org/10.1016/j.actamat.2019.06.032.
[9] Y. Chen, Z. Xu, M. Wang, Y. Li, C. Wu, Y. Yang, A single-phase V0.5Nb0.5ZrTi refractory high-entropy alloy with outstanding tensile properties, Mater. Sci. Eng. A 792 (2020), 139774, https://doi.org/10.1016/j.msea.2020.139774.
[10] B.C. Kang, T.Y. Kong, H.J. Ryu, S.H. Hong, Superior mechanical properties and strengthening mechanisms of lightweight AlxCrNbVMo refractory high-entropy alloys (x = 0,0.5,1.0) fabricated by the powder metallurgy, J. Mater. Sci. Technol. 69 (2021) 12345, https://doi.org/10.1016/j.jmst.2020.07.012.
[11] N.N. Guo, L. Wang, L.S. Luo, X.Z. Li, Y.Q. Su, J.J. Guo, H.Z. Fu, Microstructure and mechanical properties of refractory MoNbHfZrTi high-entropy alloy, Mater. Des. 81 (2015) 87, https://doi.org/10.1016/j.matdes.2015.05.019.
[12] B. Wang, Q.Q. Wang, N. Lu, X. Liang, B. Shen, Enhanced high-temperature strength of HfNbTaTiZrV refractory high-entropy alloy via Al_2O_3 reinforcement, J. Mater. Sci. Technol. 123 (2020) 191, https://doi.org/10.1016/j.jmst.2022.01.025.
[13] T. Xiang, Z. Cai, P. Du, K. Li, Z. Zhang, G. Xie, Dual phase equal-atomic NbTaTiZr high-entropy alloy with ultra-fine grain and excellent mechanical properties fabricated by spark plasma sintering, J. Mater. Sci. Technol. 90 (2021) 150, https://doi.org/10.1016/j.jmst.2021.03.024.
[14] O.N. Senkov, G.B. Wilks, J.M. Scott, D.B. Miracle, Mechanical properties of $Nb_{25}Mo_{25}Ta_{25}W_{25}$ and $V_{20}Nb_{20}Mo_{20}Ta_{20}W_{20}$ refractory high entropy alloys, Intermetallics 19 (2011) 698, https://doi.org/10.1016/j.intermet.2011.01.004.
[15] J. Jayaraj, P. Thirathipviwat, J. Han, A. Gebert, Microstructure, mechanical and thermal oxidation behavior of AlNbTiZr high entropy alloy, Intermetallics 100 (2018) 9, https://doi.org/10.1016/j.intermet.2018.05.015.
[16] X. Yang, Y. Zhang, P.K. Liaw, Microstructure and compressive properties of $NbTiVTaAl_x$ high entropy alloys, Procedia Eng. 36 (2012) 292, https://doi.org/10.1016/j.proeng.2012.03.043.
[17] G. Yi, Y. Ding, Y. Cheng, P. Zhang, X. Wang, X. Liang, Development and oxidation behavior of high entropy silicide (NbMoTaWV)Si_2 coatings on NbMoTaWV alloy, J. Alloy. Compd. 916 (2022) 65384, https://doi.org/10.1016/j.jallcom.2022.165384.
[18] G. Stéphane, P.C. Jean, D.B. Miracle, From high-entropy alloys to complex concentrated alloys, C. R. Phys. 19 (2018) 721, https://doi.org/10.1016/j.crhy.2018.09.004.
[19] T.E. Whitfield, H.J. Stone, C.N. Jones, N.G. Jones, Microstructural degradation of the $AlMo_{0.5}NbTa_{0.5}TiZr$ Re-metal high-entropy superalloy at elevated temperatures, Entropy 23 (2021) 80, https://doi.org/10.3390/e23010080.
[20] Z. Cheng, W. Yang, D. Xu, S. Wu, X. Yao, Y. Lv, J. Chen, Improvement of high temperature oxidation resistance of micro arc oxidation coated $AlTiNbMo_{0.5}Ta_{0.5}Zr$ high entropy alloy, Mater. Lett. 262 (2020), 127192, https://doi.org/10.1016/j.matlet.2019.127192.
[21] S. Lu, X. Li, X. Liang, J. He, W. Shao, K. Li, J. Chen, Effect of Y additions on the oxidation behavior of vacuum arc melted refractory high-entropy alloy $AlMo_{0.5}NbTa_{0.5}TiZr$ at elevated temperatures, Vacuum 201 (2022), 111069, https://doi.org/10.1016/j.vacuum.2022.111069.
[22] O.N. Senkov, S.V. Senkov, C. Woodward, Effect of aluminium on the microstructure and properties of the refractory high- entropy alloys, Acta Mater. 68 (2014) 214, https://doi.org/10.1016/j.actamat.2014.01.029.
[23] S. Lu, X.X. Li, X. Liang, W. Shao, W. Yang, J. Chen, Effect of Al content on the oxidation behavior of refractory high-entropy alloy $AlMo_{0.5}NbTa_{0.5}TiZr$ at elevated temperatures, Int. J. Refract. Het 105 (2022), 105812, https://doi.org/10.1016/j.ijrmhm.2022.105812.
[24] C. Deng, C. Wang, L. Chai, T. Wang, J. Luo, Mechanical and chemical properties of $CoCrFeNiMo_{0.2}$high entropy alloy coating fabricated on Ti6Al4V by laser cladding, Intermetallics 144 (2022), 107504, https://doi.org/10.1016/j.intermet.2022.107504.
[25] H. Wu, S. Zhang, C.H. Zhang, H.T. Chen, J. Chen, New studies on wear and corrosion behavior of laser cladding $FeNiCoCrMo_x$ high entropy alloy coating: The role of Mo, Int. J. Refract. Hard. Met. 102 (2022), 105721, https://doi.org/10.1016/j.ijrmhm.2021.105721.
[26] K. Böör, R. Qiu, A. Forslund, O. Bäcke, H. Larsson, E. Lindahl, M. Halvarsson, M. Boman, L.V. Fieandt, Chemical vapor deposition of TiN on a CoCrFeNi multi-principal element alloy substrate, Surf. Coat. 393 (2020), 125778, https://doi.org/10.1016/j.surfcoat.2020.125778.
[27] J.S. Han, B. Su, J. Meng, A. Zhang, Y. Wu, Microstructure and composition evolution of a fused slurry silicide coating on MoNbTaTiW refractory high-entropy alloy in high-temperature oxidation environment, Materials 13 (2020) 3592, https://doi.org/10.3390/ma13163592.
[28] W. Yang, K. Choi, C. Choi, J.S. Park, Degradation properties of refractory MoNbTaVW high-Entropy alloys with simultaneous Si/Al pack cementation coatings under high-temperature flame tests, Oxid. Met. 96 (2021) 557–569, https://doi.org/10.1007/s11085-021-10072-5.
[29] K. Choi, W. Yang, K.H. Baik, Y.M. Kim, S. Lee, S.Y. Lee, J.S. Park, Growth kinetics and isothermal oxidation behavior of a Si pack cementation-coated Mo-Si-B alloy, Appl. Surf. Sci. 489 (2019) 668, https://doi.org/10.1016/j.apsusc.2019.06.020.
[30] J.H. He, X.P. Guo, Y.Q. Qiao, F. Luo, A novel Zr-Y modified silicide coating on NbSi based alloys as protection against oxidation and hot corrosion, Corros. Sci. 177 (2020), 108948, https://doi.org/10.1016/j.corsci.2020.108948.
[31] J. Kuang, P. Zhang, Z. Hu, X. Liang, B. Shen, Formation and oxidation behavior of refractory high- entropy silicide (NbMoTaW)Si_2 coating, Corros. Sci. 198 (2022), 110134, https://doi.org/10.1016/j.corsci.2022.110134.
[32] S. Majumdar, I. Sharma, I. Samajdar, P. Bhargava, Relationship between pack chemistry and growth of silicide coatings on Mo-TZM alloy, J. Electrochem. Soc. 155 (2008) D734, https://doi.org/10.1149/1.2987954.
[33] Z.D. Xiang, P.K. Datta, Relationship between pack chemistry and aluminide coating formation for low-temperature alienization of alloy steels, Acta Mater. 54 (2006) 4453, https://doi.org/10.1016/j.actamat.2006.05.032.
[34] S.R. Levine, R.M. Caves, Thermodynamics and Kinetics of Pack Aluminide coating formation on IN-100, J. Electrochem. Soc. 121 (1974) 1051, https://doi.org/10.1149/1.2401976.
[35] W. Yang, K. Choi, K.H. Baik, Y.M. Kim, S. Lee, J.M. Kim, J.W. Lee, J.S. Park, Oxidation behaviors of Si/Al pack cementation coated Mo–3Si–1B alloys at various temperatures, Met. Mater. Int. 21 (2021) 914, https://doi.org/10.1007/s12540-019-00471-4.
[36] H. Zahedi, F.S. Nogorani, M. Safari, Microstructure analysis of the pack cementation aluminide coatings modified by CeO_2 addition, Met. Mater. Int. 27 (2021) 922, https://doi.org/10.1007/s12540-019-00483-0.
[37] M. Qian, D. Shan, Y. Ji, D. Li, J. Xu, W. Li, K. Chen, Transition of carrier transport behaviors with temperature in phosphorus-doped Si nanocrystals/SiO_2 multilayers, Nanoscale Res. Lett. 11 (2016) 346, https://doi.org/10.1186/s11671-016-1561-z.

[38] S. Li, F. Chen, F. Lin, Y. Kong, H. Dai, Adsorption performance of SiO_2/CPAM composites for aqueous Ca (II), BioRes. 13 (2018) 3554, https://doi.org/10.15376/biores.13.2.3554-3570.
[39] T. Tago, N. Kataoka, H. Tanaka, K. Kinoshita, XPS study from a clean surface of Al_2O_3 single crystals, Procedia Eng. 216 (2017) 175, https://doi.org/10.1016/j.proeng.2018.02.081.
[40] A. Pedone, Properties calculations of silica-based glasses by atomistic simulations techniques: a review, J. Phys. Chem. 113 (2009) 20773–20784, https://doi.org/10.1021/jp9071263.